Finite Element Analysis of Porous Commercially Pure Titanium for Biomedical Implant Application

Nicolas Soro, Laurence Brassart, Yunhui Chen, Martin Veidt, Hooyar Attar, Matthew S. Dargusch

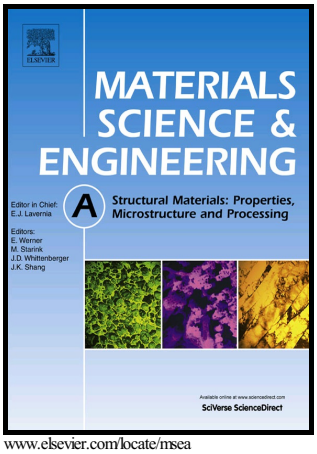

www.elsevier.com/locate/msea

PII: S0921-5093(18)30506-9
DOI: https://doi.org/10.1016/j.msea.2018.04.009
Reference: MSA36329

To appear in: *Materials Science & Engineering A*

Received date: 14 February 2018
Revised date: 3 April 2018
Accepted date: 3 April 2018

Cite this article as: Nicolas Soro, Laurence Brassart, Yunhui Chen, Martin Veidt, Hooyar Attar and Matthew S. Dargusch, Finite Element Analysis of Porous Commercially Pure Titanium for Biomedical Implant Application, *Materials Science & Engineering A,* https://doi.org/10.1016/j.msea.2018.04.009

Finite Element Analysis of Porous Commercially Pure Titanium for Biomedical Implant Application

Nicolas Soro[a*], Laurence Brassart[b], Yunhui Chen[a], Martin Veidt[a], Hooyar Attar[a], Matthew S. Dargusch[a,c*]

[a]*Centre for Advanced Materials Processing and Manufacturing (AMPAM), School of Mechanical and Mining Engineering, The University of Queensland, Brisbane, QLD 4072, Australia*

[b]*Department of Materials Science and Engineering, Monash University, VIC 3800, Australia*

[c]*ARC Research Hub for Advanced Manufacturing of Medical Devices*

n.soro@uq.edu.au

m.dargusch@uq.edu.au

[*]*Corresponding authors.*

ABSTRACT

In biomedical implant applications, porous metallic structures are particularly appealing as they enhance the stiffness compatibility with the host tissue. The mechanical properties of the porous material are critically affected by microstructural features, such as the pore shape, the distribution of porosity, and the level of porosity. In this study, mechanical properties of porous commercially pure titanium structures with various porosity levels were investigated through a combination of experiments and finite element modelling. Finite element simulations were conducted on representative volume elements of the microstructure to assess the role of pore parameters on the effective mechanical properties. Modelling results indicated that the shape of the pore, in addition to porosity level, play a significant role on the effective behaviour. Finite element simulations provide reasonably accurate prediction of the effective Young's modulus, with errors as low as 0.9% for porosity of 35%. It was observed that the large spread in yield strength produced by the simulations was most likely due to the

random pore distribution in the network, which may lead to a high probability of plastic strain initiation within the thin walls of the porous network.

Keywords: Finite element analysis; Micromechanical modelling; Porous titanium; Biomaterial

1 Introduction

Metallic materials are good candidates for tissue engineering and biomedical applications that require load-bearing capacity [1]. Titanium and its alloys are particularly attractive due to their very good biocompatibility and good corrosion resistance. Although they have lower elastic modulus compared to typical metallic biomaterials (Co-Cr alloys and 316 Stainless Steel), their high stiffness compared to human bones remains a concern to date [2]. This elastic modulus mismatch induces a load redistribution near the implant (the stress-shielding effect), which may lead to bone resorption and, eventually, implant loosening. This type of loosening is the main cause of revision surgery, driving research efforts in the development of new metallic biomaterials with tailored properties [3]. The two most common approaches to this problem are the use of alloying elements [4-6] and/or porous structures [7-9], which can both decrease the elastic modulus of the material. Open porous structures are also advantageous for biological fixation and provide an appropriate environment for complete bone ingrowth and vascularization [10].

Porous metals can be manufactured with a wide range of techniques such as powder metallurgy [11-13], gas foaming [14], casting [15] and 3D metal printing [8, 16]. However,

these techniques can be associated with technical difficulties introduced by the relatively high-melting point of titanium and its chemical reactions with some gases [17]. Moreover, spherical powders are usually required for 3D metal printing technologies such as selective laser melting, which makes the process costly. The space holder method, which consists of compacting and sintering a mixture of powders, is one of the simplest manufacturing techniques for porous titanium. The low processing cost has also made this method very appealing. The level of porosity, pore size and pore shape can all be controlled during this manufacturing process [18].

In a recent study, Chen *et al.* [19] demonstrated that the use of sugar pellets as a space holder material in a titanium matrix has good potential for hard tissue engineering. The observed interconnected porous network as well as the relatively spherical pore shape are both features which promote good implant durability. However, the mechanical properties of these porous materials have not yet been characterized, and structure-property relationships remain to be elucidated.

Given the importance of the elastic properties in tissue engineering applications, predictive mechanical models that can relate these properties to the underlying microstructure are strongly desirable. This can be addressed by full-field simulations on a Representative Volume Element (RVE) of the microstructure, typically using the Finite Element (FE) method. This approach has been extensively used to predict the effective properties of composite materials [20, 21] and porous structures, including biomaterials [22-25], and is often used as a reference to verify the predictions of simplified analytical schemes. The advantage of this approach is that it is suited to arbitrary geometries and material behaviour. The drawback is that the RVE size of random microstructure may be large, which may lead to prohibitive computational cost. For example, Shen *et al.* [26] investigated the compressive behaviour of porous titanium with the FE method. In that study, the constraints in term of

meshing limited the authors to study low porosity only (17% porosity) with no overlapping pores and conventional prescribed-displacement boundary conditions. As an alternative to full-field simulations, the RVE problem can be solved using mean-field (MF) approximations [27], such as the popular Mori-Tanaka model [28, 29], which require very low computational cost. While initially proposed for linear elastic behaviour, extensions to elasto-plastic behaviour have been proposed before [30]. However, the accuracy of MF models is not guaranteed for complex microstructures or non-linear behaviour. When applied to porous materials, they are usually limited to low-to-moderate porosity levels (0-20%) [22, 25].

In this work, FE simulations are used to predict and understand the mechanical behaviour of porous materials under uniaxial compressive loading. RVEs of the random microstructures include various porosity levels and two pore shapes (spherical and spheroidal pores). Simulations are conducted both in elasticity and elasto-plasticity, and the numerical predictions are compared to experimental data. Local deformation mechanisms are also investigated through the FE simulations.

2 Experimental procedure

This work considers porous materials produced by compaction and sintering of titanium powder and using sugar pellets as space holders. The processing technique was proposed by Chen *et al.* [17] and the resulting materials were found promising for biomedical applications. The same procedure was adopted here, and the main aspects of the experimental procedure are represented here, as they guided the modelling assumptions. More detail regarding the protocol can be found in the original publication [19].

2.1 Sample preparation

Commercially pure titanium powder was mixed with sugar pellets space holders for 30 min using a GlenMills Turbula mixer. Porosity was adjusted by varying the relative volume

fractions of titanium and sugar pellets. The volume fraction of sugar pellets is taken as the nominal pore volume fraction. Porous materials with two porosity levels were produced, with the volume fractions of both powders reported in Table 1. As a reference, dense titanium samples were also produced with the same process. Lower porosities (under 20% porosity) were excluded, as they lead to stiff materials, and higher porosities (above 50% porosity) were excluded due to manufacturing complexity.

Table 1. The specification of the titanium samples designed for fabrication.

Sample Name	% Volume of Ti	% Volume of Sugar
Ti_Dense	100	0
Ti_30	70	30
Ti_40	60	40

The sugar pellets had a particle size comprised between 300μm and 425μm, which is within the recommended pore size for bone scaffolds [3, 23]. The titanium powder consists of particles ranging between 40μm and 50μm. After mixing the powder to the desired porosity ratio, the powder was compacted to 600MPa through a Carver Manual Hydraulic press to produce cylindrical samples. Pilot experiments have shown that such a high pressure is required to avoid disintegration of the sample during the dissolution of the sugar pellets. The green body was then placed into warm water (85°C) for 4 hours to dissolve the sugar pellets. Finally, the samples were sintered using a Carbolite high vacuum furnace at 1250°C for 2 hours with a heating/cooling rate of 4°C/min.

2.2 Density measurements and microstructure characterization

Density measurements were conducted on sintered specimens in order to compare the actual density of the material to the targeted, nominal porosity. To this end, the Archimedes method was used as follows:

- The dry samples were first weighted in air (W_{Air})
- The samples were then impregnated in oil under pressure, so that the oil infiltrated the pores.
- The impregnated samples were weighted in air (W_{oil})
- The impregnated samples were weighted in H-Galden (W_{HG})
- The porosity was then calculated using:

$$\rho = \frac{\rho_{HG} \times W_{Air}}{W_{oil} - W_{HG}} \quad (1)$$

with ρ_{HG}=1.69g/ml at 21°C.

In order to characterize the pore shape and pore distribution, one specimen of each porosity level was cut, grinded and polished. The cross sections of the samples in both axial and radial directions were then observed using a Polyvar Met optical microscope.

2.3 Mechanical testing

Uniaxial compression tests were carried out on three specimens for each porosity level using an Instron 5584 with a crosshead speed of 0.001 mm/s at room temperature. The height-to-diameter ratio of the samples was almost 1.6 and the top and bottom surfaces were machined to ensure geometric accuracy before compression testing. The stress-strain curve from the dense titanium was used as the material input in the FE simulations while data for porous samples were taken as reference for the comparison with FE simulation results.

3 Experimental results

The following experimental observations from density measurements and pore-shape characterization have directed the modelling assumptions of this work. The data from the

mechanical testing are also introduced hereafter and will be subjected to an in-depth comparison with the computational findings in a following section.

The density measurements are given in Table 2. Similar to Chen *et al.*'s work [19], a consistent discrepancy of approximately 10% below the nominal porosity was observed. As reported previously, closed pores (i.e. not interconnected) as well as the shrinkage of pores during sintering are the reasons for these differences. The geometries used in the simulations are based on these measured porosity level.

Table 2. Young moduli and yield strengths measured experimentally and predicted by the FE models.

Material	Actual Porosity (%)	Method	Young's modulus (GPa)	Yield strength at 0.2% (MPa)
Ti_dense	--	Experimental	**91** ± 3.8	**500** ± 65
Ti_30	**27.1** ± 0.49	Experimental	**38.1** ± 6.1	**310** ± 22.8
		FEM (Spheres)	**49.6** ± 1.2	**270** ± 15.9
		FEM (Spheroids)	**42.9** ± 1.9	**245** ± 22.7
Ti_40	**35.5** ± 1.12	Experimental	**33.8** ± 2.1	**247** ± 13.2
		FEM (Spheres)	**39.3** ± 1.7	**221** ± 18.1
		FEM (Spheroids)	**33.5** ± 2	**190** ± 24.1

Representative optical images of the porous microstructure are shown in Figure 1. The pores exhibit a circular shape when the observation plane is taken perpendicular to the compaction direction (Figure 1.a). However, in a plane parallel to the direction of compaction, the pores show an elliptical shape (Figure 1.b). The high pressure of 600MPa applied prior to sintering is quite probably at the origin of this phenomenon. Based on these observations, it was assumed that the pores can be represented as oblate spheroids, with a ratio of the spheroid

short axis to its long axis estimated to be 0.72. The ratio was estimated from optical images, over numerous inclusions, in various specimens.

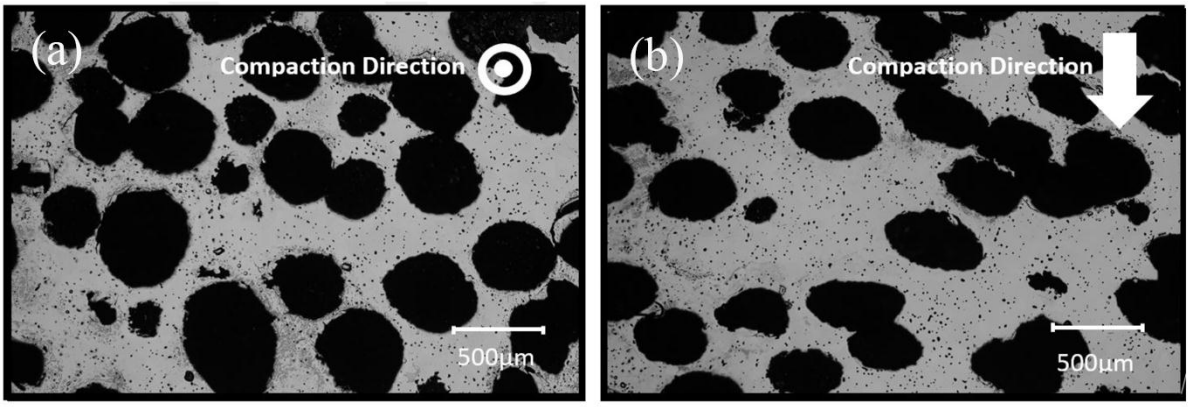

Fig 1. Optical images of 40% porous Ti sample: (a) cross-sectional view (vertical to the compaction direction) and (b) parallel to the compaction direction.

True stress-strain curves of the dense and porous samples in uniaxial compression are shown in Figure 2. As expected, porosity brings about a significant drop in both the elastic modulus and the yield strength. The average and standard deviation of these mechanical properties are presented in Table 2. The average Young's modulus of the dense titanium was found to be 91GPa. This is smaller than the value reported in the literature for commercially pure dense titanium (100 GPa) [4]. The discrepancy can be partially explained considering the microporosity commonly found in sintered titanium from unsintered particles [11]. Since this microporosity is also present in the solid matrix of the porous samples, as can be seen in Figure 1, we have considered the elastic modulus to be 91GPa for our simulations on porous samples.

The elastic moduli of the porous samples were measured at 38.1GPa for Ti_30 and 33.8GPa for Ti_40, which is relatively close to the targeted modulus of bone (1-30GPa). The average yield strengths of 310MPa and 247MPa fall well above the recommended minimal values for hard tissue engineering applications (100-180MPa) [31, 32]. While the spread in the Young's moduli of the porous samples is quite low (standard deviation of 6.1GPa and 2.1GPa for

Ti_30 and Ti_40, respectively), the large variations in yield stresses and plastic response, as illustrated in Figure 2 and Table 2, may suggest a lack of reproducibility within the manufacturing process. The variations in local phenomena associated by the random distribution of the pores may explain these disparities.

The responses from the dense samples show a smooth elastic-plastic transition, followed by significant linear hardening until failure of the material around 45% deformation (not displayed on the curves). On the other hand, the curves for the porous specimens display limited hardening past the yield point, which is most likely due to local collapse of pores within the material. For the highest porosity level of 35%, a slight softening can be observed just after the yield point. This phenomenon is associated with local damage of the material, which can be described as brittle crushing: localised damage from excessive plastic strain propagates through the porous network. Similar types of failure have been observed by Z. Liu *et al*. [33] with levels of porosity in the same range as investigated here (26% and 36%).

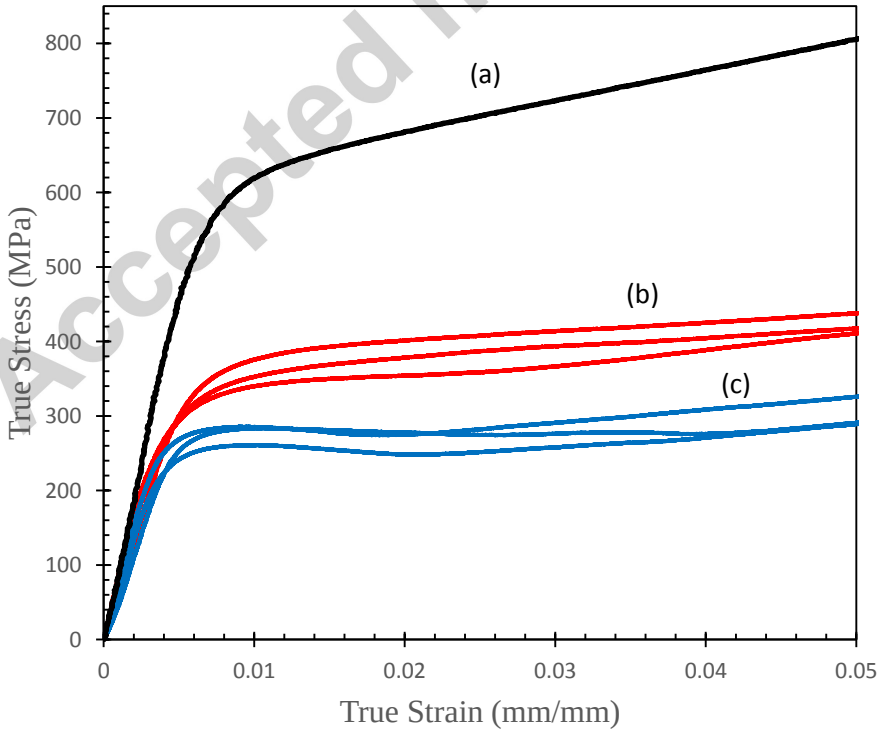

Fig 2. True stress-strain curves in uniaxial compression for (a) dense titanium (b) 27% porous titanium (Ti_30) (c) 35% porous titanium (Ti_40). For the dense material, only one representative curve was plotted from a set of 3 tests, since the three curves were very similar.

4 Micromechanical modelling

The mechanical behaviour of the porous samples was further investigated using a micromechanical approach. Specifically, finite elements simulations were conducted on RVEs of the microstructure, with boundary conditions corresponding to a given macroscopic load. As previous research has noted [20, 24], the simulation volume for random microstructures should be taken sufficiently large in order to be truly representative of the actual microstructure. Geometric features, such a pore shape, pore distribution, and volume fraction, should also be similar to the experimentally-observed features.

4.1 Generation of random porous geometries

Random porous geometries were generated by sequentially adding inclusions (i.e. pores) with random centre coordinates and given shape in a unit cube, until the targeted porosity is reached. The adopted algorithm is similar to previous work [20]. Inclusions were allowed to overlap, and periodicity was assumed. Additional constraints were introduced within this algorithm to ensure a minimal distance between non-overlapping inclusion surfaces and between the inclusion surface and the cube edges. These conditions ensure sufficient mesh quality for subsequent simulations.

The actual porosity in the model can vary slightly from the desired porosity. Since it was not possible to accurately calculate the porosity within the random sequential algorithm, the actual density was measured afterwards within the Finite Element software ABAQUS [34] by summing the volumes of the integration points in the FE mesh. The accepted discrepancy between the targeted porosity and the calculated one was ± 1%, and the accepted discrepancy between the targeted number of inclusions and the actual number of inclusions was ± 2.

Geometries with spherical pores were generated assuming that the inclusions can take two possible values of diameter, with ratio of the smallest diameter (d) to largest diameter (D) given by the ratio of diameters of the sugar pellets in the experimental setup:

$$R = \frac{D}{d} = \frac{425}{300} = 1.42 \quad (3)$$

Optical microscope observations revealed that the pores are flattened to a spheroidal shape due to the high compaction pressure applied during the manufacturing process (Figure 1). In order to investigate whether the pore shape can significantly affect the mechanical response of the material, geometries with spheroidal pores were also generated assuming that the volume of each spheroid is equal to the initial volume of the spherical space holder: $\frac{4}{3}\pi r^3 = \frac{4}{3}\pi a b^2$, with $r = d/2$ or $r = D/2$, and a and b the short and long axes of the oblate spheroid, respectively. According to the microscopy observations, the aspect ratio of the spheroid was set to $\frac{a}{b} = 0.72$.

4.2 Meshing and finite element simulations

The random geometries were meshed automatically using the software Netgen [35]. The software creates periodic meshes that allow using periodic boundary conditions afterwards. Finite element simulations were conducted with the software ABAQUS [34], using C3D4 elements (first order tetrahedral elements). Second order elements have been considered but these were subjected to various errors and complications in term of node ordering and element distortion when converting the mesh generated by Netgen in ABAQUS format. An example of undeformed mesh for a RVE with 30 spherical inclusions is illustrated in Figure 3.

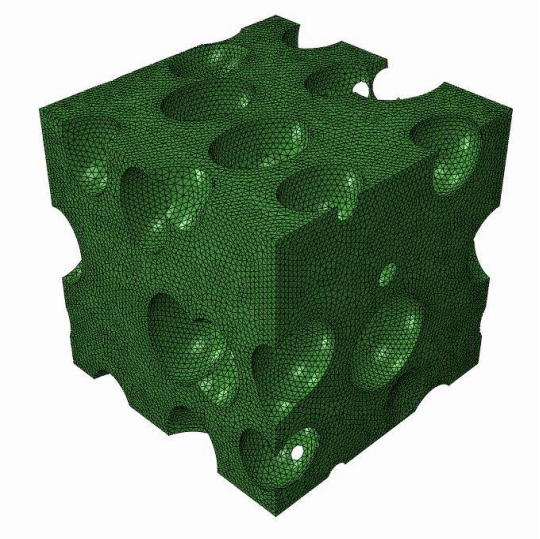

Fig 3. Example of a 27% porous RVE with spheroidal inclusions.

The behaviour of bulk titanium was described by classical von Mises plasticity theory. The Young modulus was set to the experimental value of 91 GPa, and the Poisson ratio was set to 0.33, which is a common value for sintered titanium [36, 37]. The hardening behaviour was extracted from the experimental curve for bulk titanium (Fig. 2) and specified in ABAQUS.

Periodic conditions corresponding to a given macroscopic strain tensor $\bar{\varepsilon}_{ij}$ are defined as follows:

$$u_i^+ - u_i^- = \bar{\varepsilon}_{ij}(x_j^+ - x_j^-)$$

where $\bar{\varepsilon}_{ij}$ is the macroscopic strain, x_i^+ and x_i^- are the coordinates of corresponding boundary nodes on either side of the RVE, and u_i^+ and u_i^- their displacements. These boundary conditions insure that the volume average of the strain field in the RVE and the macroscopic strain coincide:

$$\bar{\varepsilon}_{ij} = \frac{1}{V}\int \varepsilon_{ij} dV,$$

where V is the RVE volume. The macroscopic stress tensor $\bar{\sigma}_{ij}$ corresponding to a prescribed macroscopic strain is calculated from direct volume averaging of the microscopic stress field as:

$$\bar{\sigma}_{ij} = \frac{1}{V}\int \sigma_{ij} dV$$

For simulating uniaxial compression tests, only the axial component of the macroscopic strain is known, and the other components are calculated iteratively such that the corresponding components of macroscopic stress vanish.

4.2 Determination of the RVE size

In order to define an appropriate RVE size giving a good compromise between accuracy and cost-effectiveness, a convergence analysis was conducted to study the influence of the simulation volume on the elastic modulus. (By volume size, we actually mean the number of inclusions, or pores, within the volume.) In the case of randomly distributed pores, different realisations of the same geometry (i.e. same porosity and same pore shape) should give close estimates of the effective mechanical properties, and these should tend to the theoretical value when the volume size tends to infinity, in order for the volume to be considered as a true RVE. Prior to this study, the mesh itself was subjected to a convergence study and the element size was kept small enough to ensure numerical convergence for all subsequent simulations. Eight number of inclusions were successively considered, taking spherical inclusions and a fixed R-ratio (Eq. (3)). For each prescribed number of inclusions, five realisations of the random geometry were generated, and the effective Young modulus was taken as the average of the Young moduli obtained for these five realisations. Results are summarized in Table 3.

Table 3. Predicted Young modulus as a function of the inclusion number. The inclusions have a spherical shape.

Averaged Porosity (%)	No. of Inclusions	Averaged Young's Modulus (GPa)	Standard Deviation on Young's Modulus (GPa)
27.9	3	49.71	4
29.2	6	46.80	2.12
29.2	12	48.66	2.64
28.7	18	47.60	0.63
27.6	24	49.05	1.72
28	30	48.79	1.39
28.2	36	49.01	0.90
28.1	42	48.85	0.84

Figure 4 shows the evolution of the average Young modulus as a function of the number of inclusions in the simulation volume. The standard deviation of the elastic modulus generally decreases as the number of inclusion increases, and the average modulus tends to a constant value. While the models with three inclusions seem unusable due to a large spread in the results (approximately 20%), the models with 30 inclusions or more show relatively low dispersion (from 8% to 3%). As a comparison, Pierard et al. found that 30 inclusions was the minimum required for a 3D RVE in his computational study on elasto-plastic composite materials [20]. In this work, all the model predictions were generated using a number of inclusions above 30 to ensure that the simulation volume can be considered as a RVE. It should be noted that all reported values of elastic moduli are always the average over five different model configurations.

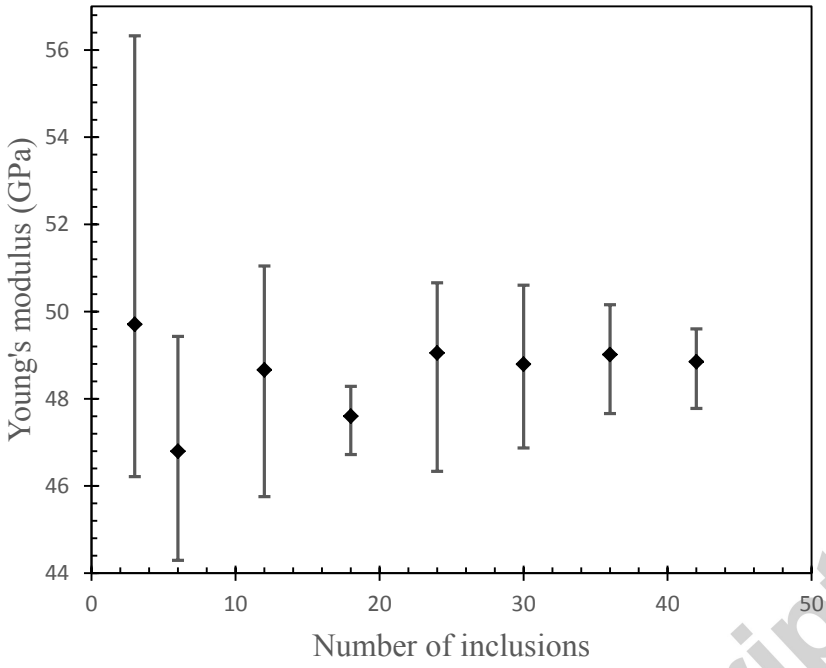

Fig 4. Predicted Young's modulus as a function of the number of inclusions in the FE simulation, for a targeted porosity of 27%. Averages and standard deviations were calculated based on five realisations of random microstructures for each number of inclusion.

5 Numerical results and discussion

5.1 Elastic properties

The predicted evolution of the Young modulus with porosity is presented in Figure 5 for both spherical and spheroidal inclusions (solid lines), together with experimental data (black squares). Although the evolution of the Young modulus follows similar behaviour for both inclusion shapes, the discrepancy between the two curves is significant, and increases with the porosity, with 9% difference for the lowest considered porosity, and up to 23% for the highest considered porosity. Numerical values for the experimental values of the porosity are also reported in Table 3. The results show that the more realistic representation of pores by spheroids gives much better agreement with the experimental data, with predicted Young moduli respectively of 42.9GPa for Ti_30 and 33.5GPa Ti_40, while the experimental data obtained were 38.1GPa and 33.8GPa. This corresponds to a 12.5% difference for Ti_30, and to a much lower difference of 0.9% for Ti_40.

Overestimation of elastic moduli with FE models were also observed by González and Nuno [38] in their FE study. These authors attributed the discrepancy to geometric irregularities in the material, in this case 3D printed, which are not accounted for in the FE model. Campoli et al. [25] also found that FE models overestimate the experimental data and demonstrated that the structural irregularities can strongly influence the mechanical response of porous materials. In the present case of space holder manufacturing process, the irregularities can emanate from the sintering process itself as well as contamination of the material by undissolved spherical pellets.

The uncertainty in the measured porosity levels may also be at the origin of discrepancies. At low porosity levels, closed pores may not be considered with the density measurement approach used in this work. This may explain the larger error observed for the lowest porosity studied here. At high porosity, the probability of closed isolated pores becomes lower, as discussed in ref [11], which should make the density measurement more and more accurate as the porosity increases. Furthermore, we have considered the pores as spheroids with a unique R-ratio (Eq (3)). While this ratio has been estimated over numerous inclusions from optical microscopy, it is in reality likely to differ slightly throughout the material. This heterogeneous distribution could potentially affect the macroscopic mechanical response. Hypothetical premature plasticity as well as damage in the samples could also have an impact on the overall behaviour of the material.

The main drawback of the FE simulations is their computational cost. As a comparison, we also considered the predictions of the classical linear Mori-Tanaka model, which assumes that the inclusion phase (here, the pores) can be represented by a single inclusion embedded in an infinite matrix and subjected to the matrix average strain as far-field strain [29]. This also means that the Mori-Tanaka model does not account for the overlapping of the pores. Expressions for the Mori-Tanaka estimate for inclusions of ellipsoidal shape can be found in

the literature [29] and are not reported here. As shown in Figure 5, the mean-field approximations (dashed lines) show large discrepancies compared to the FE reference predictions, with a clear overestimation of the Young's moduli. This difference also increases with porosity, which confirms that mean-field approximates are only reliable at low to moderate porosity. (ie. up to 20% porosity)

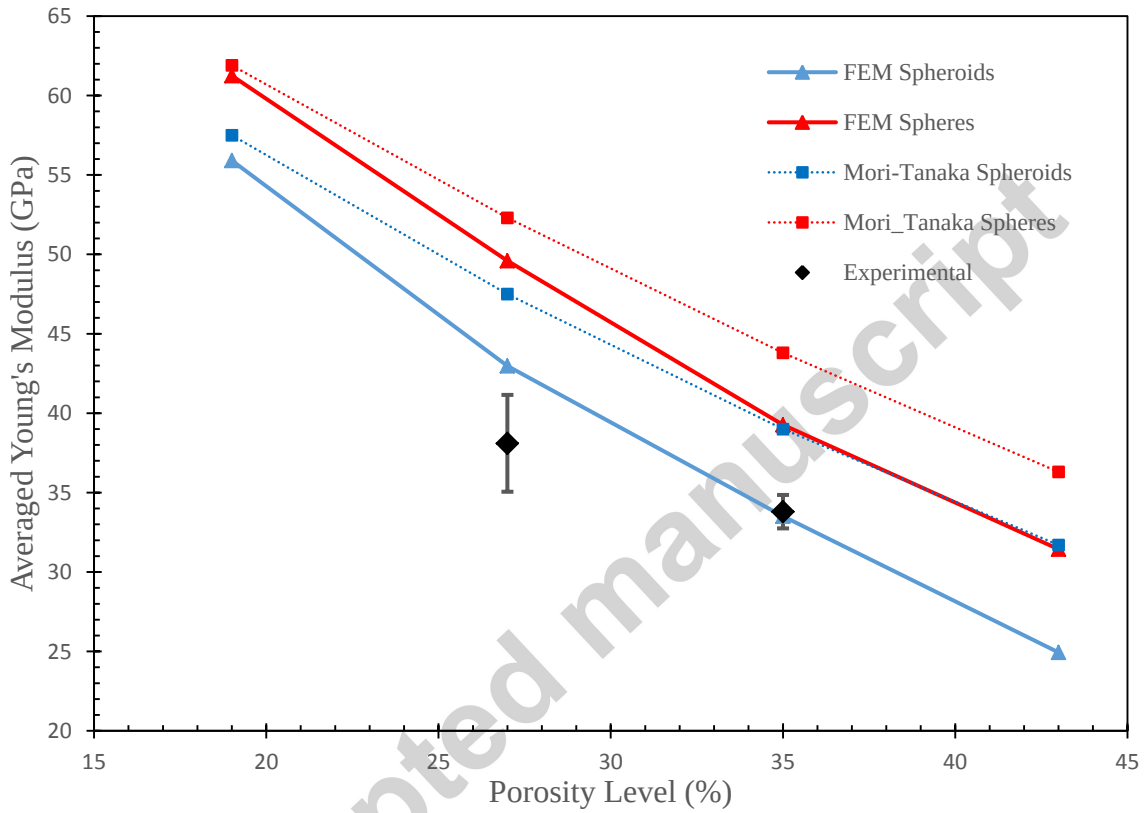

Fig 5. Evolution of the axial Young's modulus with porosity as predicted by the FE demo (solid lines) and the Mori-Tanaka model (dashed lines). The black squares are the experimental data.

5.2 Plastic response

Figure 6 compares true stress-strain curves extracted from the FE simulations for spheroidal inclusions to a representative experimental one. The average and standard deviations of the

predicted yield strength are reported in Table 2. A large variability in the numerical predictions can be observed as well as an overall underestimation of the yield points for both levels of porosity. It is most likely that the computational models generated for the simulations contain sharper geometries than those found in the experimental samples, especially in the overlapping areas. Indeed, the reduction in surface energy that happens during the sintering process might minimise the probability of sharp edges in the porous network [39]. The sharper geometries in the models would then induce an early plasticity from excessive stress concentrations. The relatively large standard deviation on the yield stress observed in the response of the dense titanium, as reported in Table 2, could also explain the underestimated computational prediction.

Unlike the numerical predictions, experimental data shows a limited hardening past the yield points, a phenomenon that could be explained from the lack of damage criterion as well as failure mode within the simulations. As previously mentioned, the brittle crushing of the material is characterised by successive collapsing at different locations, which is reflected in the plastic plateau that tends to have a limited hardening (if no hardening at all) in the experimental data.

The relatively wide distribution of the predicted yield values and plastic responses suggests that the simulation volumes can no longer be considered as true RVEs in the plastic regime. While the RVE size has been chosen to ensure convergence for the elastic constants, the high sensitivity on the plastic strain from localised stress concentrations might require a larger RVE in order to reach convergence in plasticity. Previous studies have shown similar outcomes with large variability on the numerical simulations regarding the plastic response of porous metals [26, 36]. This issue might also be at the origin of the overall underestimation of the yield strengths for the porous samples.

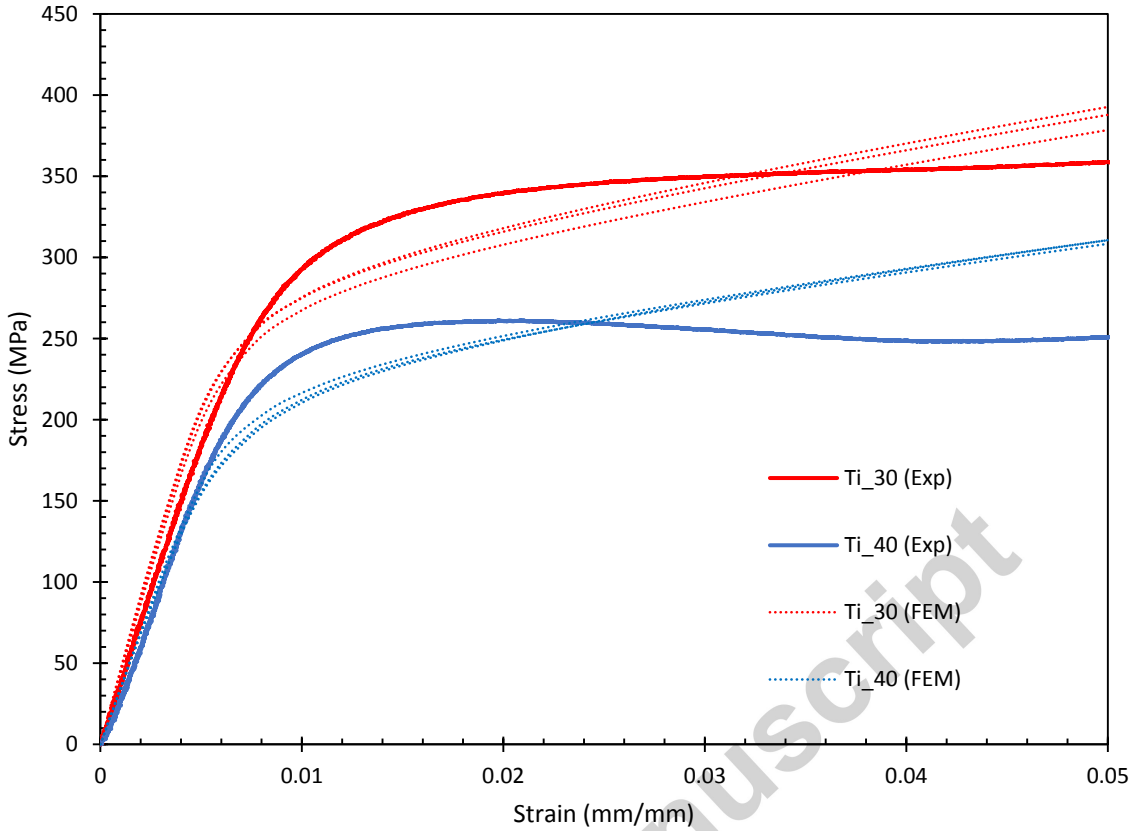

Fig 6. True stress-strain curves from FE simulations on three different RVEs with spheroidal inclusions and corresponding representative experimental results.

5.3 Local fields

Figure 7 shows the micro fields of the models after compression of 5% strain. For both levels of porosity, clear stress concentrations can be observed. These stress concentrations are likely to be at the origin of the wide variation in the plastic behaviour in the FE simulations. The von Mises stresses are found to be well above the initial yield strength of the material for a relatively low strain of 5%. Thus, they induce localised plastic deformation, occurring mostly within the thin walls of the structures, that is, where two pores are very close to each other, a scenario that is most likely to happen giving the random distribution brought about by the manufacturing process. In addition, it is expected that the probability of thin walls within the network increases with the increase in porosity [26]. Highly localised plasticity is likely to result in damage of the material, which could explain the absence of hardening capacity

observed in the experimental curves. Damage, however, is not taken into account in our simulations. Figure 8 illustrates an example of how the effective plastic strain develops within the porous network, which may suggest the collapsing pattern in the network.

With the models developed in this study, the concentration factor shows relatively high values (above 2 for the Ti_40 models). Therefore, highly porous titanium (above 50%) using this manufacturing process may be out of reach when considering the high probability of stress concentration, the high concentration factor and the difficulty in manufacturing itself. Similar observations were made Schen et al. [26] and Maiti et al. [40] regarding these stress concentrations in stochastic foams. To overcome this issue, new manufacturing methods such as additive manufacturing have emerged in the production of porous material [25, 41], providing flexibility on overall shape as well as internal architectures. Even though being more costly, the manufactured regular structures can then provide a more homogeneous response in terms of stress, minimizing the probability of early failure and providing a better strength to weight ratio. [40]

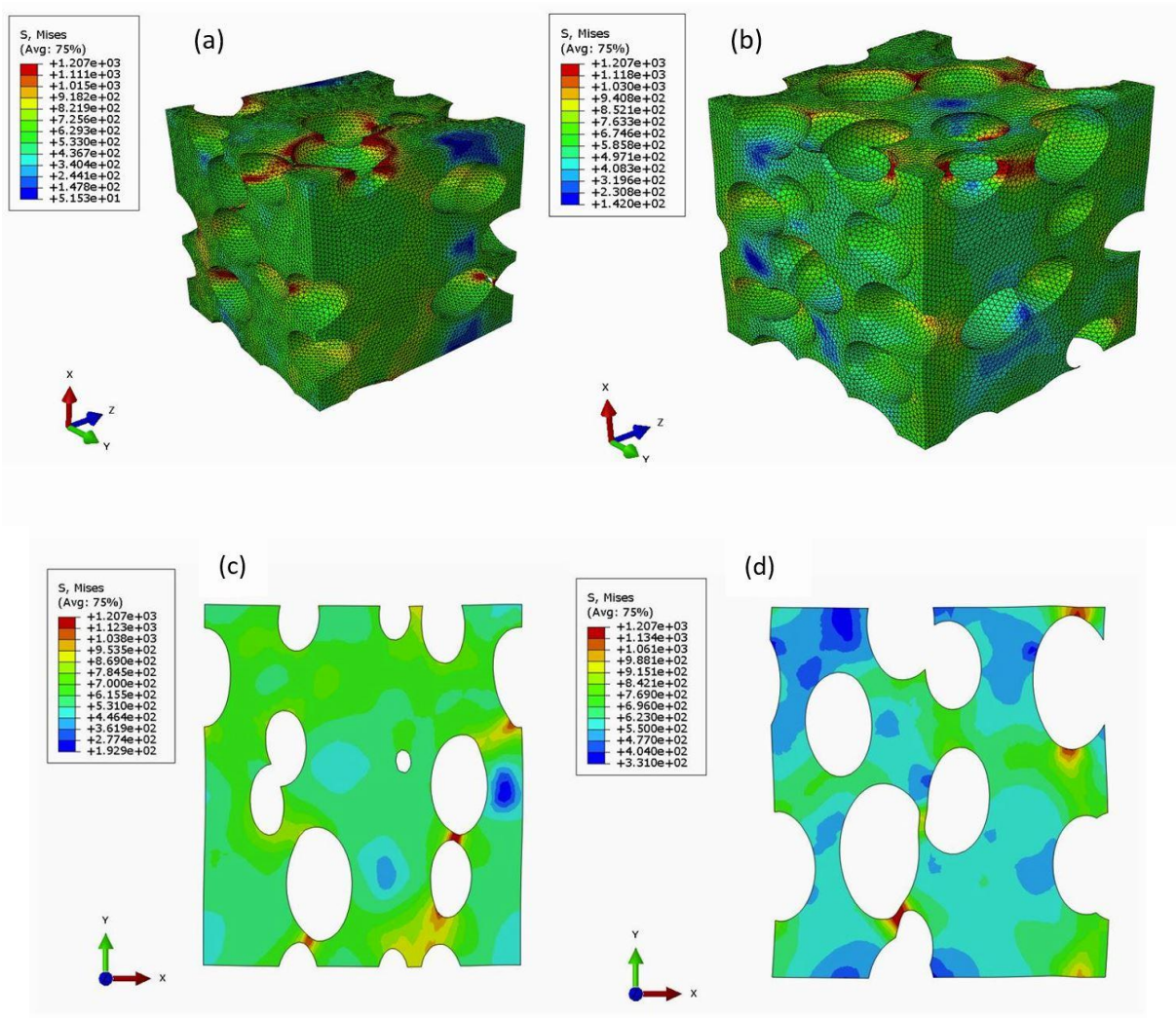

Fig 7. Contour plots of the von Mises stress (in MPa) at 5% strain and (a) 27% porosity (b) 35% porosity. The 2D slices were extracted from the 3D simulations for (c) 27% porosity and (d) 35% porosity.

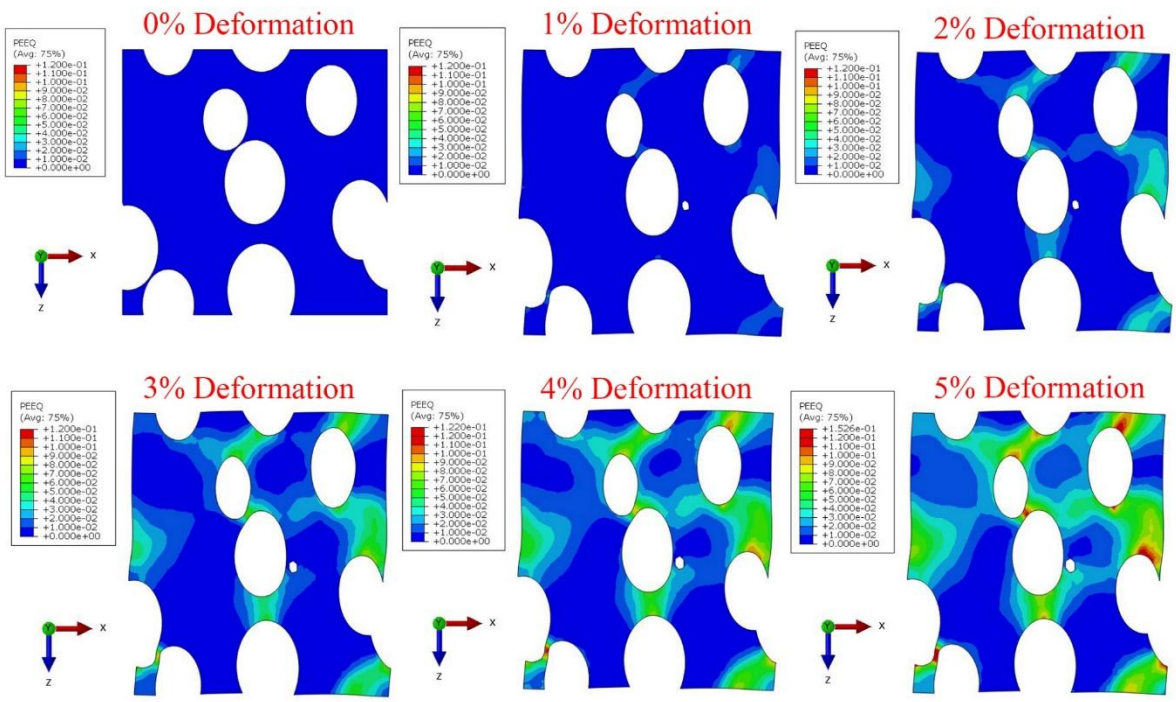

Fig 8. Evolution of the effective plastic strain for a 35% porous RVE. (Compression in x direction)

5.4 Anisotropic properties

Optical images and differences in mechanical response between spherical and ellipsoidal pore shapes both suggest a transverse isotropy for the produced material. While the experimental setup only allowed us to characterize the Young modulus in the axial direction, the FE model may be used to predict the other elastic constants and quantify the level of anisotropy to be expected in the produced materials.

For transverse isotropy, three loading scenarios are necessary to obtain all five independent elastic constants: compression along the axial direction (x-axis), compression along the transverse direction (y-axis) and pure shear in the xy plane. The effective elastic constants for RVEs with spheroidal inclusions are reported in Table 5. The anisotropy is quite pronounced, and can be quantified by the relative difference between the Young moduli in the axial and radial directions. This anisotropy ratio increases with porosity, ranging from 12% to 22% between the lowest (19%) and highest (43%) considered porosity levels.

Table 4. Averaged elastic constants for transverse isotropy as predicted by the FE model.

Porosity Level	E_x (GPa)	E_y (GPa)	v_{xy}	v_{yz}	G_{xy} (GPa)
19%	55.9	63.7	0.282	0.305	22.8
27%	42.9	53.4	0.258	0.296	18.3
35%	33.5	41.2	0.244	0.281	14.6
43%	24.9	31.8	0.235	0.255	11.1

Conclusion

Finite element simulations were used to understand and predict the mechanical behaviour of novel porous titanium materials produced by sintering. It was found that the spheroidal pore shape brought about by the manufacturing process has a significant impact on both the Young's modulus and yield strength. This also leads to anisotropy in the elastic properties, and the degree of anisotropy (as measured by the relative difference in the axial and transverse Young moduli) can reach up to 22% for porous structures with 40% porosity. The consideration of oblate spheroidal pores in the FE simulations also leads to better agreement with the experimental data, as compared to spherical pores. As expected, the FE results also demonstrated better predictive capabilities than the semi-analytical Mori-Tanaka model.

Analysis of the local fields predicted by the FE simulations also revealed high stress concentrations and localised plastic deformation in the thin walls of the porous structures. These stress and strain concentrations are likely to lead to local premature damage of the material, which is supported by the loss of the hardening capacity observed in the experimental curves. The randomly distributed pore network resulting from the manufacturing process is likely to present such thin walls, and the probability increases with porosity. These observations support the need for regular internal architectures that could minimize the stress concentrations and provide better strength to weight ratio.

In conclusion, the adopted modelling approach showed good potential for predicting the stiffness of porous titanium under compressive loading, a major property for biomedical applications. It also emphasised the importance of having better control on the pore shape and pore distribution during the manufacturing process, as these can easily lead to anisotropic properties and stress concentrations.

Acknowledgements

The authors acknowledge the support of Queensland Centre for Advanced Materials Processing and Manufacturing (AMPAM). They are also grateful to Dr. Damon Kent for his technical support. N. Soro, H. Attar and M. S. Dargusch would like also to acknowledge the support of the Australian Research Council through the ARC Research Hub for transforming Australian industry through Additive Manufacturing (IH130100008). Professor Dargusch would also like to acknowledge the support of ARC Research Hub for Advanced Manufacturing of Medical Devices (IH150100024).

References

[1] S. H. Teoh, *Engineering materials for biomedical applications* vol. 1: World scientific, 2004.

[2] M. Geetha, A. Singh, R. Asokamani, and A. Gogia, "Ti based biomaterials, the ultimate choice for orthopaedic implants–a review," *Progress in materials science,* vol. 54, pp. 397-425, 2009.

[3] Y. Li, C. Yang, H. Zhao, S. Qu, X. Li, and Y. Li, "New Developments of Ti-Based Alloys for Biomedical Applications," *Materials,* vol. 7, p. 1709, 2014.

[4] S. Guo, Q. Meng, X. Zhao, Q. Wei, and H. Xu, "Design and fabrication of a metastable β-type titanium alloy with ultralow elastic modulus and high strength," *Scientific reports,* vol. 5, 2015.

[5] M. Akita, Y. Uematsu, T. Kakiuchi, M. Nakajima, Y. Bai, and K. Tamada, "Fatigue behavior of bulk β-type titanium alloy Ti–15Mo–5Zr–3Al annealed in high temperature nitrogen gas," *Materials Science and Engineering: A,* vol. 627, pp. 351-359, 2015.

[6] Y. Abd-elrhman, M. A.-H. Gepreel, A. Abdel-Moniem, and S. Kobayashi, "Compatibility assessment of new V-free low-cost Ti–4.7 Mo–4.5 Fe alloy for some biomedical applications," *Materials & Design,* vol. 97, pp. 445-453, 2016.

[7] G. He, P. Liu, and Q. Tan, "Porous titanium materials with entangled wire structure for load-bearing biomedical applications," *Journal of the mechanical behavior of biomedical materials,* vol. 5, pp. 16-31, 2012.

[8] X. Wang, S. Xu, S. Zhou, W. Xu, M. Leary, P. Choong*, et al.*, "Topological design and additive manufacturing of porous metals for bone scaffolds and orthopaedic implants: A review," *Biomaterials,* vol. 83, pp. 127-141, 3// 2016.

[9] B. Lee, T. Lee, Y. Lee, D. J. Lee, J. Jeong, J. Yuh*, et al.*, "Space-holder effect on designing pore structure and determining mechanical properties in porous titanium," *Materials & Design,* vol. 57, pp. 712-718, 2014.

[10] J. Matena, S. Petersen, M. Gieseke, A. Kampmann, M. Teske, M. Beyerbach*, et al.*, "SLM produced porous titanium implant improvements for enhanced vascularization and osteoblast seeding," *International journal of molecular sciences,* vol. 16, pp. 7478-7492, 2015.

[11] Y. Chen, J. E. Frith, A. Dehghan-Manshadi, H. Attar, D. Kent, N. D. M. Soro*, et al.*, "Mechanical properties and biocompatibility of porous titanium scaffolds for bone tissue engineering," *Journal of the Mechanical Behavior of Biomedical Materials,* vol. 75, pp. 169-174, 2017.

[12] M. Yan, M. Qian, C. Kong, and M. Dargusch, "Impacts of trace carbon on the microstructure of as-sintered biomedical Ti–15Mo alloy and reassessment of the maximum carbon limit," *Acta biomaterialia,* vol. 10, pp. 1014-1023, 2014.

[13] W. Niu, C. Bai, G. Qiu, and Q. Wang, "Processing and properties of porous titanium using space holder technique," *Materials Science and Engineering: A,* vol. 506, pp. 148-151, 2009.

[14] H. J. Kim, I. K. Park, J. H. Kim, C. S. Cho, and M. S. Kim, "Gas foaming fabrication of porous biphasic calcium phosphate for bone regeneration," *Tissue Engineering and Regenerative Medicine,* vol. 9, pp. 63-68, 2012.

[15] H. R. Ramay and M. Zhang, "Preparation of porous hydroxyapatite scaffolds by combination of the gel-casting and polymer sponge methods," *Biomaterials,* vol. 24, pp. 3293-3302, 2003.

[16] H. Attar, L. Löber, A. Funk, M. Calin, L. Zhang, K. Prashanth*, et al.*, "Mechanical behavior of porous commercially pure Ti and Ti–TiB composite materials manufactured by selective laser melting," *Materials Science and Engineering: A,* vol. 625, pp. 350-356, 2015.

[17] D. C. Dunand, "Processing of Titanium Foams," *Advanced Engineering Materials,* vol. 6, pp. 369-376, 2004.

[18] B. Arifvianto and J. Zhou, "Fabrication of metallic biomedical scaffolds with the space holder method: a review," *Materials,* vol. 7, pp. 3588-3622, 2014.

[19] Y. Chen, D. Kent, M. Bermingham, A. Dehghan-Manshadi, and M. Dargusch, "Manufacturing of biocompatible porous titanium scaffolds using a novel spherical sugar pellet space holder," *Materials Letters,* vol. 195, pp. 92-95, 2017.

[20] O. Pierard, C. Gonzalez, J. Segurado, J. LLorca, and I. Doghri, "Micromechanics of elasto-plastic materials reinforced with ellipsoidal inclusions," *International Journal of Solids and Structures,* vol. 44, pp. 6945-6962, 2007.

[21] T. Kanit, S. Forest, I. Galliet, V. Mounoury, and D. Jeulin, "Determination of the size of the representative volume element for random composites: statistical and numerical approach," *International Journal of solids and structures,* vol. 40, pp. 3647-3679, 2003.

[22] M. El Ghezal, Y. Maalej, and I. Doghri, "Micromechanical models for porous and cellular materials in linear elasticity and viscoelasticity," *Computational Materials Science,* vol. 70, pp. 51-70, 2013.

[23] V. Karageorgiou and D. Kaplan, "Porosity of 3D biomaterial scaffolds and osteogenesis," *Biomaterials,* vol. 26, pp. 5474-5491, 2005.

[24] J. Alsayednoor, "Modelling and characterisation of porous materials," University of Glasgow, 2013.

[25] G. Campoli, M. Borleffs, S. A. Yavari, R. Wauthle, H. Weinans, and A. A. Zadpoor, "Mechanical properties of open-cell metallic biomaterials manufactured using additive manufacturing," *Materials & Design,* vol. 49, pp. 957-965, 2013.

[26] H. Shen and L. Brinson, "Finite element modeling of porous titanium," *International Journal of Solids and Structures,* vol. 44, pp. 320-335, 2007.

[27] S. Nemat-Nasser and M. Hori, *Micromechanics: overall properties of heterogeneous materials* vol. 37: Elsevier, 2013.

[28] T. Mori and K. Tanaka, "Average stress in matrix and average elastic energy of materials with misfitting inclusions," *Acta metallurgica,* vol. 21, pp. 571-574, 1973.

[29] Y. Benveniste, "A new approach to the application of Mori-Tanaka's theory in composite materials," *Mechanics of materials,* vol. 6, pp. 147-157, 1987.

[30] I. Doghri and A. Ouaar, "Homogenization of two-phase elasto-plastic composite materials and structures: study of tangent operators, cyclic plasticity and numerical algorithms," *International Journal of Solids and structures,* vol. 40, pp. 1681-1712, 2003.

[31] S.-I. Roohani-Esfahani, P. Newman, and H. Zreiqat, "Design and fabrication of 3D printed scaffolds with a mechanical strength comparable to cortical bone to repair large bone defects," *Scientific reports,* vol. 6, p. 19468, 2016.

[32] Y. Torres, P. Trueba, J. Pavón, E. Chicardi, P. Kamm, F. García-Moreno, *et al.*, "Design, processing and characterization of titanium with radial graded porosity for bone implants," *Materials & Design,* vol. 110, pp. 179-187, 2016.

[33] Z. Liu, F. Ji, M. Wang, and T. Zhu, "One-Dimensional Constitutive Model for Porous Titanium Alloy at Various Strain Rates and Temperatures," *Metals,* vol. 7, p. 24, 2017.

[34] Hibbitt, Karlsson, and Sorensen, *ABAQUS/standard User's Manual* vol. 1: Hibbitt, Karlsson & Sorensen, 2001.

[35] J. Schöberl, "NETGEN An advancing front 2D/3D-mesh generator based on abstract rules," *Computing and visualization in science,* vol. 1, pp. 41-52, 1997.

[36] S. Muñoz, J. Pavón, J. Rodríguez-Ortiz, A. Civantos, J. Allain, and Y. Torres, "On the influence of space holder in the development of porous titanium implants: Mechanical, computational and biological evaluation," *Materials Characterization,* vol. 108, pp. 68-78, 2015.

[37] M. Thieme, K.-P. Wieters, F. Bergner, D. Scharnweber, H. Worch, J. Ndop, *et al.*, "Titanium powder sintering for preparation of a porous functionally graded material destined for orthopaedic implants," *Journal of materials science: materials in medicine,* vol. 12, pp. 225-231, 2001.

[38] F. J. Q. Gonzalez and N. Nuno, "Finite element modeling of manufacturing irregularities of porous materials," *Biomaterials and Biomechanics in Bioengineering,* vol. 3, pp. 1-14, 2016.

[39] R. M. German, "Sintering Trajectories: Description on How Density, Surface Area, and Grain Size Change," *JOM,* vol. 68, pp. 878-884, 2016.

[40] A. Maiti, W. Small, J. Lewicki, T. Weisgraber, E. Duoss, S. Chinn, *et al.*, "3D printed cellular solid outperforms traditional stochastic foam in long-term mechanical response," *Scientific reports,* vol. 6, p. 24871, 2016.

[41] J. J. Lewandowski and M. Seifi, "Metal additive manufacturing: a review of mechanical properties," *Annual Review of Materials Research,* vol. 46, pp. 151-186, 2016.

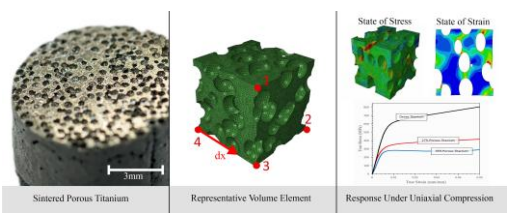

Graphical Abstract